# Halo Mass-concentration Relation at the High-mass End

Weiwei Xu, Huanyuan Shan, Ran Li, Chunxiang Wang, Linhua Jiang, Eric Jullo, Ginevra Favole, Jean-Paul Kneib, Chaoli Zhang

The Astrophysical Journal, 922:162 (10pp), 2021 December 1 https://doi.org/10.3847/1538-4357/ac1b9e


# Halo Mass-concentration Relation at the High-mass End

Weiwei Xu[1], Huanyuan Shan[2,3], Ran Li[4], Chunxiang Wang[4], Linhua Jiang[1], Eric Jullo[5], Ginevra Favole[6], Jean-Paul Kneib[6], and Chaoli Zhang[7]
[1] Kavli Institute for Astronomy and Astrophysics, Peking University, Beijing 100871, People's Republic of China; wwxu@pku.edu.cn
[2] Shanghai Astronomical Observatory, Chinese Academy of Sciences, Shanghai 200030, People's Republic of China; hyshan@shao.ac.cn
[3] University of Chinese Academy of Sciences, Beijing 100049, People's Republic of China
[4] National Astronomical Observatory, Chinese Academy of Sciences, Beijing 100101, People's Republic of China
[5] Aix-Marseille Université, CNRS, CNES, LAM, F-13388 Marseille, France
[6] Institute of Physics, Laboratory of Astrophysics, Ecole Polytechnique Fédérale de Lausanne (EPFL), Observatoire de Sauverny, 1290 Versoix, Switzerland
[7] College of Computer Science and Artificial Intelligence, Wenzhou University, 325035 Wenzhou, People's Republic of China
*Received 2021 March 28; revised 2021 August 2; accepted 2021 August 5; published 2021 November 29*

## Abstract

The concentration–mass ($c$–M) relation encodes key information about the assembly history of dark matter halos. However, its behavior at the high mass end has not been measured precisely in observations yet. In this paper, we report the measurement of the halo $c$–M relation with the galaxy–galaxy lensing method, using the shear catalog of the Dark Energy Camera Legacy Survey (DECaLS) Data Release 8, which covers a sky area of 9500 deg$^2$. The foreground lenses are selected from the redMaPPer, LOWZ, and CMASS catalogs, with halo masses ranging from $10^{13}$ to $10^{15}\,M_\odot$ and redshifts ranging from $z = 0.08$ to $z = 0.65$. We find that the concentration decreases with the halo mass from $10^{13}$ to $10^{14}\,M_\odot$, but shows a trend of upturn after the pivot point of $\sim 10^{14}\,M_\odot$. We fit the measured $c$–M relation with the concentration model $c(M) = C_0 \left(\frac{M}{10^{12}\,M_\odot/h}\right)^{-\gamma} \left[1 + \left(\frac{M}{M_0}\right)^{0.4}\right]$, and we get the values $(C_0, \gamma, \log_{10}(M_0)) = (5.119^{0.183}_{-0.185}, 0.205^{0.010}_{-0.010}, 14.083^{0.130}_{-0.133})$ and $(4.875^{0.209}_{-0.208}, 0.221^{0.010}_{-0.010}, 13.750^{0.142}_{-0.141})$ for halos with $0.08 \leqslant z < 0.35$ and $0.35 \leqslant z < 0.65$, respectively. We also show that the model including an upturn is favored over a simple power-law model. Our measurement provides important information for the recent argument over the massive cluster formation process.

*Unified Astronomy Thesaurus concepts:* Weak gravitational lensing (1797); Galaxy clusters (584); Catalogs (205); Surveys (1671)

## 1. Introduction

As fundamental building blocks of the dark matter universe, halos are believed to follow a self-similar structure distribution. The most widely used density profile of dark matter halos, the NFW profile, was proposed by Navarro et al. (1995, 1996, 1997). The NFW profile's slope of density $\gamma$ is equal to 1 at the inner part and grows to 3 at the outer part. In such a model, one can define the concentration of a halo to be the ratio between the virial radius ($r_{\rm vir}$) and the characteristic radius ($r_{\rm s}$), where the density slope $\gamma(r_{\rm s}) = 2$. Given the mass and concentration, the density distribution of a halo is determined.

The halo concentration is confirmed to vary with its redshift and mass, both in observations and $N$-body simulations (e.g., Johnston et al. 2007; Shan et al. 2012, 2017; Cui et al. 2018; McClintock et al. 2019). $N$-body simulations show that the relation between concentration and mass ($c$–M relation) can be used to probe the formation and evolution history of the halo (e.g., Zhao et al. 2003a, 2003b; Bullock et al. 2001), and that the dependence of the concentration on the halo mass and redshift can be described with the power-law function, $c = \alpha(M/M_{\rm pivot})^{\beta}\ (1+z)^{\gamma}$ (e.g., Duffy et al. 2008; Bullock et al. 2001; Eke et al. 2001; Neto et al. 2007; Cui et al. 2018). Recently, however, it has been argued that the power law may not extend to the high-mass end. Some $N$-body simulations (Klypin et al. 2011, 2016; Prada et al. 2012; Ishiyama et al. 2021) predict the flattening and upturn of the $c$–M relation for massive halos, and that the location of the upturn varies with redshift, which may be due to the different formation procedure of massive halos at higher redshifts.

On the observational side, gravitational lensing is the only way to detect the profile and mass of the halo directly, without any assumption about its hydrodynamic state, symmetry, or profile. This makes gravitational lensing a unique way to get tight constraints of the structure and evolution of halos (Abbott et al. 2018, 2020; Kwan et al. 2017). Previous studies have been undertaken to constrain the $c$–M relation with a variety of data sets, such as the Dark Energy Survey (DES) Science Verification data (Melchior et al. 2017), the DES Year 1 data (McClintock et al. 2019), the DES Year 3 data (Varga et al. 2021), and the Cluster Lensing and Supernova Survey with Hubble data (CLASH; Merten et al. 2015; Sereno et al. 2015). Other studies aim to measure the X-ray concentration (Sato et al. 2000; Pointecouteau et al. 2005; Vikhlinin et al. 2006; Gastaldello et al. 2007; Buote et al. 2007; Comerford & Natarajan 2007). However, these studies usually describe the $c$–M relation with the power-law function, where the concentration decreases with the halo mass in a wide mass range.

In this paper, we measure the halo $c$–M relation with the galaxy–galaxy lensing method, using the shear catalog of the Dark Energy Camera Legacy Survey (DECaLS) Data Release 8, which covers a sky area of 9500 deg$^2$. The foreground lenses are selected from the redMaPPer, LOWZ, and CMASS catalogs, with halo masses ranging from $10^{13}$–$10^{15}\,M_\odot$ and

redshifts ranging from 0.08–0.65. Throughout the paper, we take $M_{200m}$ and $c_{200m}$ as the mass and concentration of the halo, which means the mean density in the halo is 200 times the matter background density at the same redshift. We make use of different $c$–M models to fit the data and try to investigate whether an upturn exists.

The set of cosmological parameters used is obtained from Planck Collaboration et al. (2020): the Hubble constant $H_0 = 67.4$ km s$^{-1}$ Mpc$^{-1}$; the baryon density parameter $\Omega_b h^2 = 0.0224$; the cold dark matter density parameter $\Omega_{cdm} h^2 = 0.120$; the matter fluctuation amplitude $\sigma_8 = 0.811$; the power index of the primordial power spectrum $n_s = 0.965$; and the matter density parameter $\Omega_m = 0.315$. The structure of this paper is listed as follows. In Section 2, the source and lens catalogs are described. In Section 3, the lensing signal, lensing model, and systematics are shown. In Section 4, we discuss the $c$–M relation measurement and fitting. In Section 5 and Section 6, the discussion and conclusion are shown, respectively.

## 2. Data

### 2.1. Source Catalog

The source galaxies used in our measurement are obtained from Data Release 8 (DR8) of the DECaLS survey, which is part of the Dark Energy Spectroscopic Instrument Legacy Imaging Survey (Blum et al. 2016; Dey et al. 2019). The sky coverage of DECaLS DR8 is ∼9500 deg$^2$ in $grz$ bands.

In the DECaLS DR8 catalog, the sources from the *Tractor* catalog (Lang et al. 2016) are divided into five kinds of morphologies: point sources, round exponential galaxies with a variable radius, DeVaucouleurs, exponential, and the composite model. Sources above the $6\sigma$ detection limit in any stack are kept as candidates. The ellipticity of a galaxy is estimated by a joint fitting on optical images in three bands ($g$, $r$, and $z$). Then, we model the multiplicative and additive biases by cross-matching the DECaLS sources with external shear measurements (Phriksee et al. 2020; Yao et al. 2020; Zu et al. 2021), including the Canada–France–Hawaii Telescope Stripe 82 (Moraes et al. 2014), the Dark Energy Survey (Dark Energy Survey Collaboration et al. 2016), and the Kilo-Degree Survey (Hildebrandt et al. 2017) sources.

We use the photometric redshift derived by Zou et al. (2019) with the $k$-nearest-neighbor (kNN) algorithm. The redshift of a target galaxy is derived with its $k$-nearest-neighbor in Spectral Energy Distribution space whose spectroscopic redshift is known. The photometric redshift (photo-$z$) is obtained from five photometric bands: three optical bands ($g$, $r$, and $z$) and two infrared bands ($W1$ and $W2$) from the Wide-Field Infrared Survey Explorer. We only take samples with $r < 23$ mag, resulting in a spectroscopic sample of about 2.2 million galaxies. The characteristics of the final catalog include a redshift bias of $\Delta z_{norm} = 2.4 \times 10^{-4}$, an accuracy of $\sigma_{\Delta z_{norm}} = 0.017$, and an outlier rate of about 5.1%. More details are discussed in Zou et al. (2019).

### 2.2. Lens Catalogs

We use the redMaPPer cluster catalog v6.3[8] as the lens catalog, which is obtained from the Sloan Digital Sky Survey (SDSS) DR8 (Rykoff et al. 2014). The catalog includes 26,111 clusters with richness $\lambda > 19$. In order to get the evolution of the $c$–M relation with redshift and mass, the redMaPPer cluster sample is separated into multiple redshift and richness bins, as shown in Figure 1 and Table 1. Outliers with $\lambda > 100$ are removed to get the main characteristics of the whole sample without bias from a few outliers. In this step, the 375 most massive clusters are removed, accounting for 1.4% of the full sample. Then, the sample is separated into two redshift parts, i.e., the low-$z$ sample ($0.08 \leqslant z < 0.35$, hereafter the $z1$ sample) and the high-$z$ sample ($0.35 \leqslant z < 0.65$, hereafter the $z2$ sample). The ratios of clusters in these two redshift samples are 40.3% and 59.7%, respectively. There are more clusters in the high-$z$ sample; this can partly compensate for the weakness of remote cluster signals. The cluster richness is used as the mass proxy to separate the massive and less massive clusters. Each redshift sample is further divided into five richness bins ($\lambda4$–$\lambda8$ bins), with similar cluster numbers in each bin. This similarity of cluster numbers can control unnecessary bias when we measure and compare the weak lensing signal of each bin. Using the galaxy–galaxy lensing measurement, we can further obtain the density profile of clusters with different halo masses at different redshifts.

Besides the redMaPPer catalog, we also utilize the LOWZ and CMASS catalogs from SDSS-III BOSS DR10 (Ahn et al. 2014) to constrain the $c$–M relation in the low-mass region. The redshifts of LOWZ and CMASS halos are constrained within 0.08–0.35 and 0.35–0.65, respectively, to match the redshift bins of redMaPPer halos. For these two catalogs, we take the stellar mass as the halo mass proxy and separate each catalog into three mass bins ($\lambda1$–$\lambda3$ bins), as shown in Figure 1 and Table 1. To minimize the effect of outliers, we remove halos with stellar mass or redshift outside the listed range.

## 3. Method

### 3.1. The Lensing Signal

The gravitational well of the foreground halo produces a tangential shear of the source around the foreground halo, which stretches and aligns the source images along the tangential direction. Thus, the projected mass density of the lens, $\Sigma$, is related to the azimuthally averaged tangential shear at the projected radius $R$. The relation is

$$\gamma_T = \frac{\bar{\Sigma}(<R) - \bar{\Sigma}(R)}{\Sigma_{crit}} \equiv \frac{\Delta\Sigma(R)}{\Sigma_{crit}}. \quad (1)$$

$\Delta\Sigma(R)$ is widely used to show the weak lensing signal, the reduced shear ($g$), which is defined as $g = \gamma/(1-\kappa)$, where $\kappa$ is the dimensionless surface mass density and defined as $\kappa = \Sigma(R)/\Sigma_{crit}$. In this paper, we also use $\Delta\Sigma(R)$ to show the detected signal.

The critical surface mass density, $\Sigma_{crit}$, is defined as

$$\Sigma_{crit}(z_l, z_s) = \frac{c^2}{4\pi G}\frac{D_s}{D_l D_{ls}}, \quad (2)$$

where $D_l$, $D_s$, and $D_{ls}$ are the angular diameter distances to the lens, to the source, and between the lens and the source, respectively, and $c$ is the constant of the velocity of light in a vacuum. $\Sigma_{crit}$ shows how the geometry of the lens-source system modulates the induced shear signal.

To obtain $\Delta\Sigma$, we stack lens-source pairs in 10 logarithmic comoving radii of 0.3–5 Mpc. Only sources with $z_s > z_l + 0.1$

[8] http://risa.stanford.edu/redmapper/

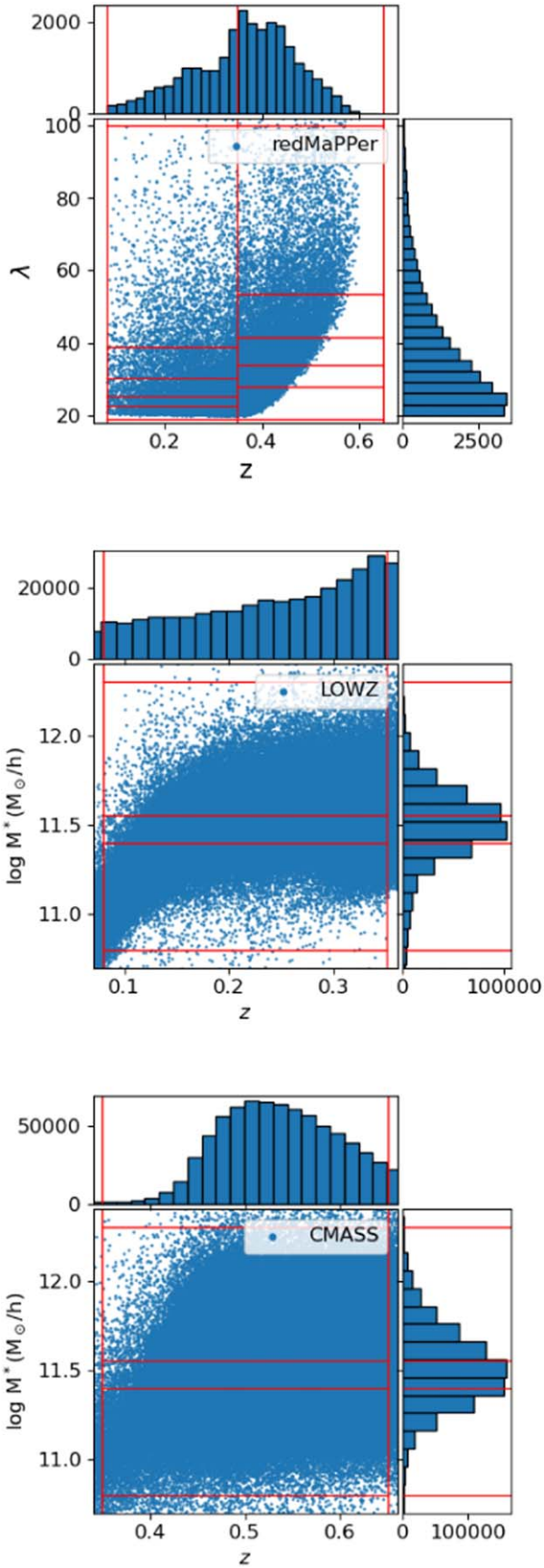


**Figure 1.** The distribution of redMaPPer, LOWZ, and CMASS samples in the redshift and mass proxy parameter space. The mass proxy is the cluster richness for redMaPPer halos and the logarithm of the stellar mass for LOWZ and CMASS halos. The red solid lines label thresholds of bins.

**Table 1**
The Details of the Redshift and Mass Proxy Thresholds for LOWZ, CMASS, and redMaPPer (Shown as "redMP.") Subsamples

| Catalog | Bin | $z$ | $\mathrm{Log}_{10}(\mathrm{M}^*)$ or $\lambda$ | $N$. | $P$.(%) |
|---|---|---|---|---|---|
| LOWZ | $\lambda 1z1$ | 0.08–0.35 | 10.80–11.40 | 97 280 | 33.4 |
| | $\lambda 2z1$ | 0.08–0.35 | 11.40–11.55 | 105 186 | 36.1 |
| | $\lambda 3z1$ | 0.08–0.35 | 11.55–12.30 | 88 648 | 30.5 |
| CMASS | $\lambda 1z2$ | 0.35–0.65 | 10.80–11.40 | 230 280 | 31.5 |
| | $\lambda 2z2$ | 0.35–0.65 | 11.40–11.55 | 225 026 | 30.7 |
| | $\lambda 3z2$ | 0.35–0.65 | 11.55–12.30 | 276 716 | 37.8 |
| redMP. | $\lambda 4z1$ | 0.08–0.35 | 19.00–22.40 | 2 078 | 8.0 |
| | $\lambda 5z1$ | 0.08–0.35 | 22.40–25.31 | 2 067 | 7.9 |
| | $\lambda 6z1$ | 0.08–0.35 | 25.31–30.15 | 2 087 | 8.0 |
| | $\lambda 7z1$ | 0.08–0.35 | 30.15–38.83 | 2 074 | 7.9 |
| | $\lambda 8z1$ | 0.08–0.35 | 38.83–100 | 2 076 | 8.0 |
| redMP. | $\lambda 4z2$ | 0.35–0.65 | 19.00–27.72 | 3 058 | 11.7 |
| | $\lambda 5z2$ | 0.35–0.65 | 27.72–33.82 | 3 078 | 11.8 |
| | $\lambda 6z2$ | 0.35–0.65 | 33.82–41.51 | 3 067 | 11.7 |
| | $\lambda 7z2$ | 0.35–0.65 | 41.51–53.37 | 3 081 | 11.8 |
| | $\lambda 8z2$ | 0.35–0.65 | 53.37–100 | 3 070 | 11.8 |

**Note.** The first column shows the catalog name. The second column lists the given name of each bin. The thresholds of redshift and mass proxy are shown in the third and fourth columns. The mass proxy is the logarithm value of stellar mass for the LOWZ and CMASS catalogs and the richness for redMaPPer. In the last two columns, the number of clusters in this bin and the bin's percentage of the whole catalog are listed.

are considered, to avoid the misclassification caused by uncertainty of the redshift. With this set of parameters, as listed in Table 2, $\Delta\Sigma(R)$ is estimated for a given set of lenses using

$$\Delta\Sigma(R) = \frac{\sum_{\rm ls} w_{\rm ls}\, \gamma_t^{\rm ls}\, \Sigma_{\rm crit}}{\sum_{\rm ls} w_{\rm ls}}, \tag{3}$$

where $\gamma_t^{\rm ls}$ is the tangential shear, $w_{\rm ls} = w_{\rm n}\Sigma_{\rm crit}^{-2}$, and $w_{\rm n}$ is the weight factor introduced to account for intrinsic scatter in ellipticity and the error of shape measurement (Miller et al. 2007, 2013). $w_{\rm n}$ used in this work is defined as $w_{\rm n} = 1/(\sigma_\epsilon^2 + \sigma_{\rm e}^2)$. $\sigma_\epsilon$ is the intrinsic ellipticity dispersion derived from the whole galaxy catalog, and taken as 0.27 (Giblin et al. 2021). $\sigma_{\rm e}$ is the error of the ellipticity measurement, defined in Hoekstra et al. (2002).

The lensing signal is recalibrated as

$$\Delta\Sigma^{\rm cal}(R) = \frac{\Delta\Sigma(R)}{1 + K(z_{\rm l})}, \tag{4}$$

and

$$1 + K(z_{\rm l}) = \frac{\sum_{\rm ls} w_{\rm ls}\,(1+m)}{\sum_{\rm ls} w_{\rm ls}}, \tag{5}$$

where $m$ is the multiplicative error as described in Section 2.1.

We use the software *SWOT*[9] (Coupon et al. 2012) to detect the stacked signal. *SWOT* is a fast tree code to compute the two-point correlations, histograms, and galaxy–galaxy lensing signals from large data sets. The *theta* projection is taken to measure the signal. The *SWOT* software can be parallelized for maximum computational efficiency. We estimate the statistical error with a Jackknife resampling of 64 subregions with equal area, and we remove one subsample at a time for each Jackknife realization. Refer to Table 2 for *SWOT* parameter settings.

[9] http://jeancoupon.com/swot.

### 3.2. The Lensing Model

We fit the observation with a comprehensive model, including the central halo, the miscentered halo, and the nearby halo term with offset.

First, we use the NFW profile to estimate the contribution from the central halo. In addition, we take into account the miscentering effect, which comes from an inaccurate determination of the halo center, and we can reduce the central signal greatly (Johnston et al. 2007). For a cluster miscentered by a distance $R_{\rm mis}$, the surface mass density is $\Sigma_{\rm mis} = \int_0^{2\pi} d\theta\ \Sigma(\sqrt{R^2 + R_{\rm mis}^2 + 2RR_{\rm mis}\cos\theta})/2\pi$. We assume a Gamma profile for the miscentering of the stacked signal (McClintock et al. 2019). The miscentering effect is characterized by two parameters, $f_{\rm mis}$ and $r_{\rm mis}$, representing the fraction of offset halos and the offset distance, respectively. Finally, we use the two-halo term to indicate the signal from nearby halos, which dominates at the cluster outskirt. The contribution from the two-halo term is estimated from the nonlinear scaling of the matter power spectrum as a function of redshift with the *Halofit* model, using the *CAMB* package.[10] For more details about the model refer to the *Cluster_toolkit* package[11] (Eisenstein & Hu 1998; Smith et al. 2003; Takahashi et al. 2012). Thus, the whole model is,

$$\Delta\Sigma(R) = (1 - f_{\rm mis})\,\Delta\Sigma_{\rm NFW}(R) + f_{\rm mis}\,\Delta\Sigma_{\rm mis}(R) + \Delta\Sigma_{\rm 2h}(R). \tag{6}$$

### 3.3. Systematics

In the model fitting, there are multiplicative corrections (McClintock et al. 2019) necessary to consider, including the boost factor ($\mathcal{B}(R)$), reduced shear ($\mathcal{G}(R)$), and photo-$z$

[10] https://github.com/cmbant/CAMB.
[11] https://cluster-toolkit.readthedocs.io/en/latest/.

**Table 2**
Parameter Settings of *SWOT*

| Para. | Value | Meaning |
|---|---|---|
| corr | gglens | Type of correlation |
| range | 0.1, 7 | Correlation range (in units of Mpc $h^{-1}$) |
| nbins | 15 | Number of bins |
| err | Jackknife | Resampling method |
| nsub | 64 | Number of resampling subvolumes |
| $H_0$ | 67.4 | Hubble parameter |
| $\Omega_m$ | 0.315 | Relative matter density |
| $\Omega_L$ | 0.684 | Relative energy density |
| $\Delta$ | 0.1 | Minimum redshift difference between the source and the lens |
| proj | como | Projection |

**Note.** The names, values, and physical meanings of parameters are listed in three columns in sequence.

bias ($\delta$). With these corrections, the observed signal is $\Delta\Sigma^{\rm cal}(R) = (1+\delta)\mathcal{G}(R)/\mathcal{B}(R)\Delta\Sigma_{\rm model}$.

#### 3.3.1. Boost Factor

The boost effect (Sheldon et al. 2004; Mandelbaum et al. 2006) comes from the membership dilution biases when some foreground or member galaxies are misclassified as background sources. If the fraction of misclassified member galaxies for the cluster is $f_{\rm cl}$, the boost factor, $\mathcal{B}(R) = (1-f_{\rm cl})^{-1}$, is used to correct the diluted signal. In this work, we use the boost factor model (Equation (7)) referring to McClintock et al. (2019), which is constructed from the NFW profile and characterized with $B_0$ and scale radius $R_s$. We use the typical values of $B_0 = 0.1$ and $R_s = 1.0$ Mpc $h^{-1}$.

$$\mathcal{B}_{\rm model}(R) = 1 + B_0\frac{1-F(x)}{x^2-1},\ (x = R/R_s) \tag{7}$$

$$F(x) = \begin{cases} \dfrac{\tan^{-1}\sqrt{x^2-1}}{\sqrt{x^2-1}} & ,(x>1) \\ 1 & ,(x=1). \\ \dfrac{\tanh^{-1}\sqrt{1-x^2}}{\sqrt{1-x^2}} & ,(x<1) \end{cases} \tag{8}$$

#### 3.3.2. Reduced Shear Error

The reduced shear error comes from the fact that the measured signal is the reduced shear ($g$), instead of the shear ($\gamma$). This can be corrected by multiplying the model with

$$\mathcal{G}(R) = \frac{1}{1-\kappa} = \frac{1}{1-\Sigma(R)\,\Sigma_{\rm crit}^{-1}}. \tag{9}$$

Here, $\Sigma(R)$ includes the contribution of the central halo, nearby halos, and the miscentering effect.

#### 3.3.3. Photo-z Bias

Besides the corrections mentioned above, we also consider the systematic uncertainties of photo-$z$ ($\delta$).

The redshift of the source is the photometric redshift estimated by the kNN algorithm (see Section 2.1), and local linear regression is used as described in Zou et al. (2019). For each galaxy, our kNN photo-$z$ algorithm provides a Gaussian estimation of the photo-$z$ error. We further apply this Gaussian scatter for each galaxy to obtain the probability distribution function (PDF) of redshift, i.e., $p_{\rm photo}(z_s)$. For each galaxy, we estimate the effective critical surface density with the redshift PDF as

$$\langle\Sigma_{\rm crit}^{-1}\rangle_{i,j} = \int dz_s\, p_{\rm phot}(z_{s,i})\,\Sigma_{\rm crit}^{-1}(z_{l,j}, z_{s,i}), \tag{10}$$

where $i$ and $j$ indicate the source and lens in a lens–source pair. For the case with $z_s < z_l$ or the offset $> 0.3$ Mpc, the value of $\langle\Sigma_{\rm crit}^{-1}\rangle_{i,j} = 0$. We only consider the signal from the lens–source pair when their projected distance is smaller than 0.3 Mpc and when the background source has a higher redshift than the foreground lens. Furthermore, we compare the kNN photo-$z$ catalog of the photometric redshift (PDF: $p_{\rm photo}^{\rm kNN}(z_s)$) with a large reliable photo-$z$ catalog (PDF: $p_{\rm photo}^{\rm true}(z_s)$) obtained from UDS HSC+SPLASH (Mehta et al. 2018), ECDF-S (Cardamone et al. 2010), CFHTLS Deep + WIRDS (Bielby et al. 2010), and COSMOS (Laigle et al. 2016). As a result, the bias of photo-$z$ is given as

$$1+\delta = \frac{\Sigma_{\rm crit,kNN}^{-1}}{\Sigma_{\rm crit,true}^{-1}}. \tag{11}$$

## 4. Result

The final parameters are estimated with the Markov Chain Monte Carlo (MCMC) fitting method using the *EMCEE* package[12] (Foreman-Mackey et al. 2013). We use 50 chains with an original length of 30,000 steps each, and discard the first 10,000 steps, similar to the implementation in Yang et al. (2020). The first parts of our chains are discarded to avoid the effects from first guesses of parameters. The relations between mass and concentration, obtained from the stacked signal of halos in the redMaPPer, CMASS, and LOWZ catalogs, are shown in Figure 3. All three lens samples are divided into two redshift bins. And in each redshift bin, there are five mass bins for redMaPPer clusters and three mass bins for CMASS and LOWZ galaxies. The criteria are shown in Table 1.

### 4.1. c–*M* Relation Measurement

For performance of signals, only signals with errors smaller than 100% are used. We measure the signal in 15 logarithmic bins in the radius of 0.1–7 Mpc, and only fit the 10 bins in 0.3–5 Mpc, to avoid the contributions of the central galaxy and nearby halos. We use the maximum likelihood fitting method to calculate best parameters in the fitting. There are four parameters to estimate: halo mass ($M_{200m}$), concentration ($c_{200m}$), offset distance ($r_{\rm mis}$), and ratio of halo with offset ($f_{\rm mis}$).

First, we fit the model with the MCMC method. Gaussian priors are assumed for the halo mass and concentration, whose central value and full width at half maximum (FWHM) are listed in Table 3. The $r_{\rm mis}$ and $f_{\rm mis}$ are assumed with flat priors within 0–1 Mpc and 0–1, respectively, with initial starting values both set as 0.2. Second, the four parameters are fitted with the MCMC method again, and all four priors are assumed to be a Gaussian distribution, with the central value and the FWHM set as the best-fit results in the previous step. Third,

[12] https://emcee.readthedocs.io/en/stable.

**Table 3**
Gaussian Priors of the Mass and Concentration of Halos from the redMaPPer, LOWZ, and CMASS Catalogs

| Samp. | $\log_{10}(M)$ | $c$ |
|---|---|---|
| redMP. | [14.5, 1.0] | [4.0, 0.5] |
| LOWZ, CMASS | [13.5, 1.0] | [4.5, 0.5] |

**Note.** For each sample, we list the central value and FWHM of the Gaussian function.

$r_{\rm mis}$ and $f_{\rm mis}$ are fixed to the best-fit values obtained from the second step. And the mass and concentration of the halo are fitted with the MCMC method, with priors listed in Table 3. Fourth, the mass and concentration are assigned Gaussian priors, with the central value and FWHM estimated from the third step. Finally, the halo mass is fixed to the value obtained in the fourth step, and the concentration is fitted with the MCMC method, with the Gaussian prior from the fourth step.

In Figure 2, we show the MCMC fitting result of the $z1\lambda6$ sample, step by step, as an example. The fitting result for steps 1, 2, 3, 4, and 5 described in the last paragraph are shown in sequence in the figure, and the final fitting is shown in the last panel. The corresponding $\chi^2/\nu$ is labeled out for each fitting.

### 4.2. c–M Relation Fitting

We fit the relation between the concentration and mass of halos with the model with upturn (K16 model; shown in Equation (12), referring to Equation (24) in Klypin et al. 2016), and the power-law model (PL model; shown in Equation (13)),

$$c(M) = C_0 \left(\frac{M}{10^{12}\, M_\odot/h}\right)^{-\gamma} \left[1 + \left(\frac{M}{M_0}\right)^{0.4}\right], \quad (12)$$

$$c(M) = C_0 \left(\frac{M}{M_0}\right)^{-\gamma}. \quad (13)$$

To remove the effect of redshift, we fit the data with two redshift bins separately. In this step, we first estimate parameters with the maximum likelihood method. Then, the best-fit parameters are obtained using the MCMC fitting method. We assume parameters ($C_0$, $\gamma$, $M_0$) as Gaussian priors whose central values are obtained from the maximum likelihood fitting, and whose FWHMs are [2, 0.13, 1], respectively. In terms of the MCMC fitting setup, we take 50 chains with lengths of 30,000 steps, with only the last 20,000 steps taken into account. In Figure 3, we show the best-fit K16 model (top panel) and the best-fit PL model (bottom panel) for samples in two redshift bins. The best-fit parameters are listed in Table 4. The reduced $\chi^2$ for both $z1$ and $z2$ for the K16 model are smaller than the values obtained from the PL model. Thus, the K16 model is a better model to describe the $c$–M relation.

## 5. Discussion

### 5.1. Comparison with Previous Observations

There are several studies dedicated to measuring the halo mass and concentration. In this section, we make a brief introduction of some previous studies, followed by the comparison with our work. A summary of these studies is shown in Table 5.

Mandelbaum et al. (2008) performed the statistical weak lensing analysis around the halos of 170,640 isolated galaxies, 38,236 groups, and 13,823 maxBCG clusters. It includes halos from galaxy size to cluster size, with masses of $10^{12}$–$10^{15}\, M_\odot\, h^{-1}$. The estimated NFW concentration parameter $c_{200b}$ decreases from ∼10 to 4 with the halo mass. They fit the $c$–M relation with the power-law function, and find that the slope is in agreement with theoretical predictions. However, their value of the measured concentration is slightly smaller than the theoretical prediction and some other measurements. Millennium simulations predict that the concentration becomes constant at higher mass ranges than the highest mass bin in their observation, and they only fit observation with the power-law relation in the work. Using WebPlotDigitizer[13] (Rohatgi 2020), we extract the data points used in their Figure 5. We discard the two leftmost and the rightmost data points because of the limited display. From these data points, we estimate the median uncertainties of the halo mass and concentration to be $\sim 8.7 \times 10^{12}\, M_\odot\, h^{-1}$ and ∼3.00, respectively.

Covone et al. (2014) obtain the stacked shear profile of ∼2000 optical-selected galaxy clusters with the shear catalog from the CFHTLenS. The whole sample is divided into six richness bins to obtain the stacked shear profiles separately. These bins correspond to $M_{200}$ from 0.48 to $3.21 \times 10^{14}\, M_\odot\, h^{-1}$. The redshift coverage is 0.1–0.6. According to the fitting result listed in their Table 1, the median constraints of the halo mass and concentration are within $0.185 \times 10^{14}\, M_\odot\ \mathrm{h}^{-1}$ and 5.4. In the model fitting of the measurements, they take into account the theoretical ΛCDM models of hierarchical structure growth. The best-fit slope is consistent with Duffy et al. (2008), and the normalization differs within $1\sigma$ error.

In the work of Umetsu et al. (2014), they made a joint shear-and-magnification weak-lensing analysis. A sample of 16 X-ray-regular and 4 high-magnification galaxy clusters selected from CLASH are taken into account. The redshift spans a range between 0.19 and 0.69. Their result also agrees with the ΛCDM prediction, especially the model of Meneghetti & Rasia (2013). However, they did not fit the measurements with the model with upturn. And the limited number of stacked clusters and the limited coverage of halo masses makes it difficult to distinguish the power-law model and the model with upturn.

With 19 X-ray selected galaxy clusters from CLASH, Merten et al. (2015) derived a new constraint of the $c$–M relation. The redshift of this sample covers 0.19–0.89. Their estimation of the $c$–M relation agrees with the theoretical estimation at a 90% confidence level. Using the combination of lensing reconstruction techniques of weak and strong lensing, they made a tight constraint of the mass and concentration, with uncertainties of $0.8 \times 10^{14}\, M_\odot/h$ and 1.0, respectively. The observation matches well with the full sample of Meneghetti & Rasia (2013), and is similar to Bhattacharya et al. (2013). However, there is also no fitting of the measurement with the model with upturn, and the limited sample impedes an accurate constraint of the $c$–M relation.

In Shan et al. (2017), they constrain the $c$–M relation with redMaPPER clusters and LOWZ and CMASS galaxies. Their halo masses are $5 \times 10^{12}$–$2 \times 10^{14}\, M_\odot\, h^{-1}$. They only consider halos with redshifts of 0.2–0.4 and 0.4–0.6, including 7425 and 27,358 halos respectively. With a large sample and an accurate shear measurement from the CFHT Stripe 82 Survey, they constrain the uncertainty of halo mass within $0.06 \times 10^{14}\, M_\odot\, h^{-1}$, $0.05 \times 10^{14}\, M_\odot\ h^{-1}$, and the uncertainties of the concentration are 0.91 and 0.86 for halos in two redshift bins.

[13] https://automeris.io/WebPlotDigitizer

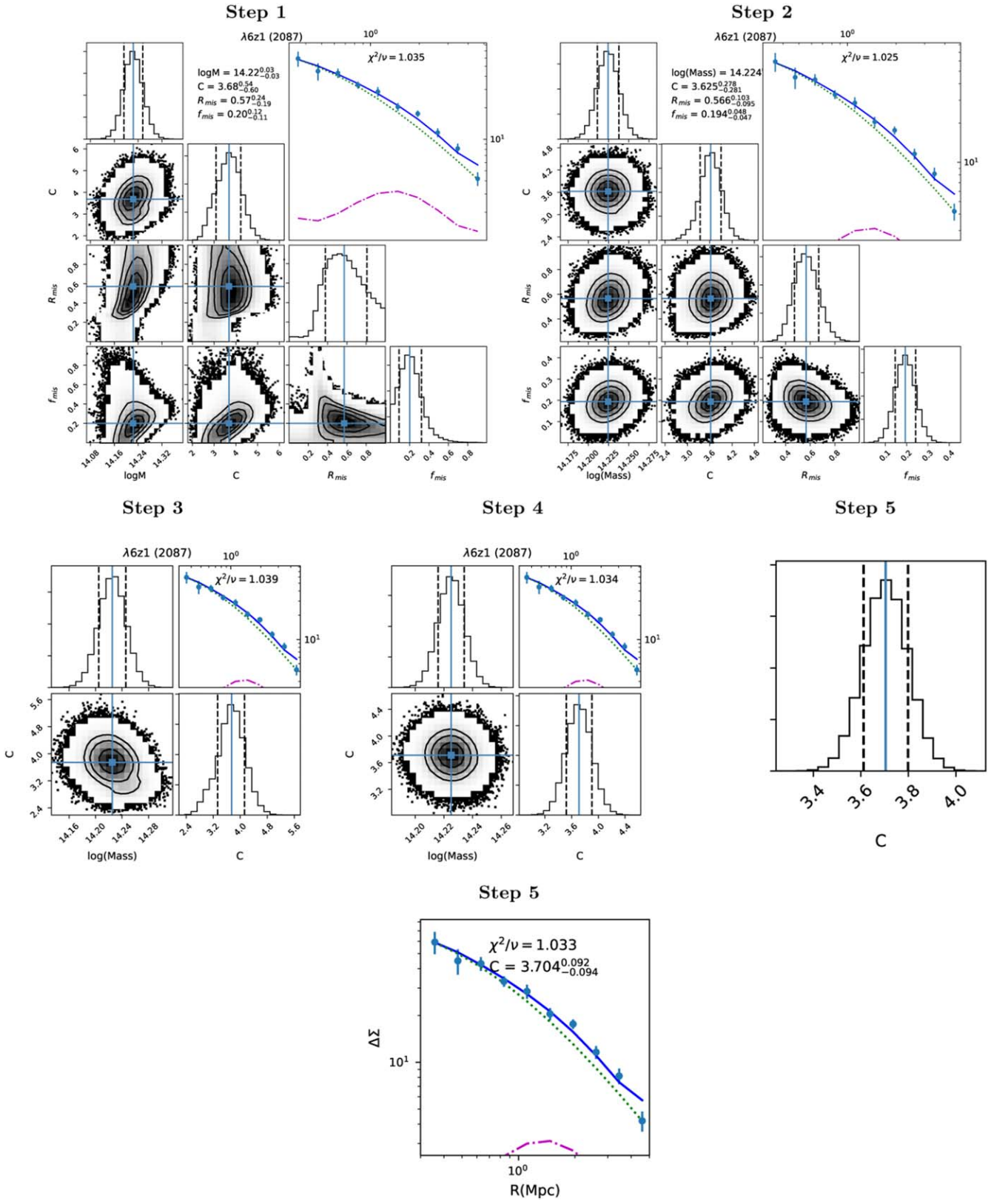


**Figure 2.** The fitting steps of $\lambda 6z1$ as an example. The first five panels correspond to steps 1–5 in Section 4.1. The last panel shows the fitting result. In the top right subpanel of each of the first two panels in the first two rows, as well as in the plot in the last row, the data and models are overlaid. The contributions from the central model, from the nearby halo plus the miscentering effect, and from the total model are shown as the green dotted curve, the magenta dashed–dotted curve, and the blue solid curve, respectively. In addition, the value of reduced $\chi^2$ is overlaid. In the panels of the first row, best-fit parameters and errors are added to the top of the second column of subpanels. The best-fit $c$ is also shown in the last panel. In each subpanel with a histogram, the median value and $1\sigma$ error are shown in solid cyan and dashed black vertical lines, respectively.

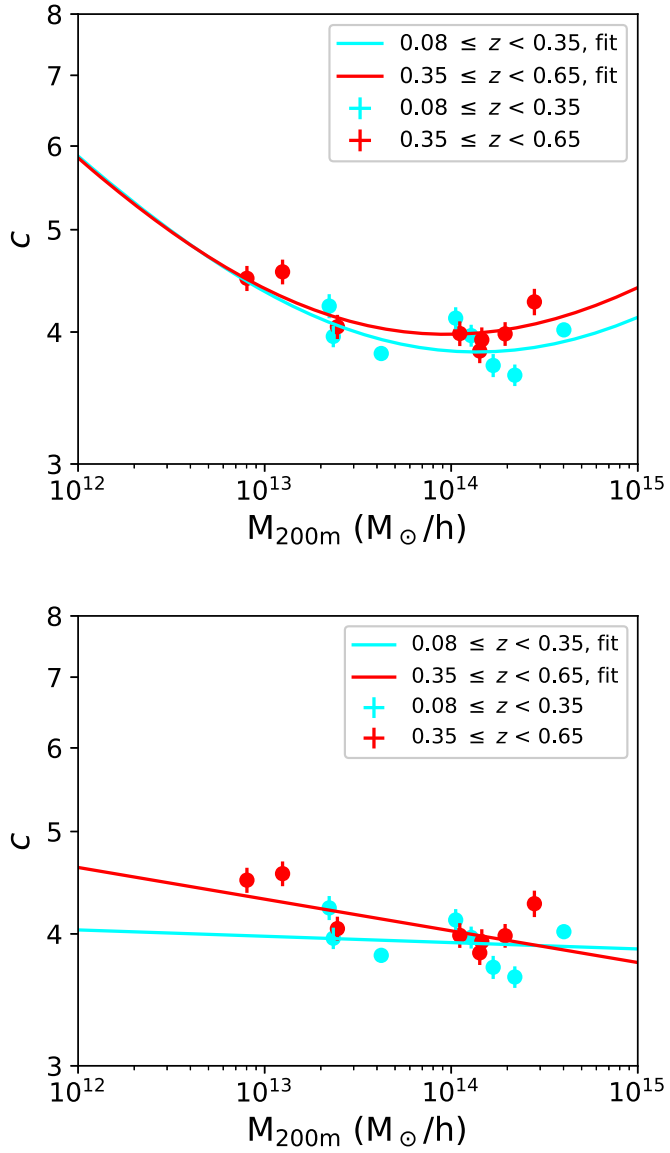


**Figure 3.** The stacked signal and model of the weak lensing of clusters. The dots with error bars are our results attained with DECaLS DR8 data, where the signal from the low-redshift sample ($z1$ sample, $0.08 \leqslant z < 0.35$) is shown in cyan, and the signal of the high-redshift sample ($z2$ sample, $0.35 \leqslant z < 0.65$) is shown in red. The solid curves are the best-fit model to the data, which are shown in the same color with the corresponding data set. The model used in the upper panel is the K16 model, while the model used in the lower panel is the PL model. The best-fit parameters are listed in Table 4. In the $z1$ and $z2$ samples, the left three data points are from the LOWZ and CMASS samples, while the other data are from the redMaPPer sample.

The measurements in two redshift bins are fitted with the power-law model, and match well with the simulation predictions (e.g., Duffy et al. 2008; Klypin et al. 2016). The comparison between the power-law model and the model with upturn is not discussed in their work.

In this work, we focus on the stacked weak lensing signal of galaxy clusters in two redshift bins ($0.08 \leqslant z < 0.35$ and $0.35 \leqslant z < 0.65$), and only consider halos with masses in the range of $5 \times 10^{12}$–$5 \times 10^{14}\, M_{\odot}\ h^{-1}$. The sample sizes are 301,496 and 747,376 for the low-redshift and high-redshift bins, respectively. Our uncertainties for halo mass are $3.08 \times 10^{12}\, M_{\odot}\ h^{-1}$ and $3.94 \times 10^{12}\, M_{\odot}\ h^{-1}$ in the low- and high-redshift bins, respectively, while the uncertainties of the concentration are 0.093 and 0.108.

Compared with previous observations, this work has the largest sample size, with more than 1 million halos taken into account. In addition, the least massive halo considered in our work ($\sim 5 \times 10^{12}\, M_{\odot}/h$) is lower than those of previous observation measurements, except Mandelbaum et al. (2008) ($\sim 5 \times 10^{11}\, M_{\odot}/h$) and Shan et al. (2017) ($\sim 5 \times 10^{12}\, M_{\odot}/h$). However, we do not consider the same very massive halos ($> 5 \times 10^{14}\, M_{\odot}/h$) as Mandelbaum et al. (2008), and Umetsu et al. (2014). Furthermore, we have a quite wide redshift coverage (0.08–0.65), which covers the whole redshift area considered in the previously mentioned studies, except for some high-redshift halos in Umetsu et al. (2014) and Merten et al. (2015). What is more important is that we make a much tighter constraint of the halo mass and the concentration, 2–10 times better than previous works.

**Table 4**
The Best-fit Parameters and $1\sigma$ Error of the $c$–M Relation

| Mod. | Samp. | $C_0$ | $\gamma$ | $\log_{10}(M_0)$ | $\chi^2/\nu$ |
|---|---|---|---|---|---|
| K16 | $z1$ | $5.119^{0.183}_{-0.185}$ | $0.205^{0.010}_{-0.010}$ | $14.083^{0.130}_{-0.133}$ | 3.610 |
| | $z2$ | $4.875^{0.209}_{-0.208}$ | $0.221^{0.010}_{-0.010}$ | $13.750^{0.142}_{-0.141}$ | 1.243 |
| PL | $z1$ | $3.915^{0.068}_{-0.069}$ | $0.006^{0.007}_{-0.007}$ | $14.177^{0.975}_{-1.016}$ | 4.983 |
| | $z2$ | $4.053^{0.266}_{-0.267}$ | $0.030^{0.009}_{-0.009}$ | $13.905^{0.996}_{-0.989}$ | 2.880 |

**Note.** The $z1$ samples refer to the samples with $0.08 \leqslant z < 0.35$, and $z2$ to the samples with $0.35 \leqslant z < 0.65$. The reduced $\chi^2$ for the K16 model and PL model are listed in the last column.

### 5.2. Comparison with Previous Cosmological Simulations

In this section, we compare our measurement in the high-redshift bin ($0.35 \leqslant z < 0.65$) with simulations at a redshift of 0.5, as shown in Figure 4. For the simulation in Zhao et al. (2009), we obtain the $c$–M relation with the halo evolution web-calculator,[14] with the power spectrum type set as *BBKS 1986 power spectrum* (Bardeen et al. 1986). We make the Kolmogorov–Smirnov test to estimate the performance of cosmological predictions. The estimation of the $p$-value for the cosmological predictions suggested in Klypin et al. (2016), Ishiyama et al. (2021) (called Uchuu simulation), Child et al. (2018), Seppi et al. (2021), Zhao et al. (2009), Duffy et al. (2008) are 0.660, 0.660, 0.087, 0.013, 0.002, and $1.554 \times 10^{-4}$, respectively. This comparison shows that the K16 model, as well as the Uchuu simulation, fit our measurement better, compared with other mentioned cosmological models.

### 5.3. Correlation between Parameters

To quantify the correlation between the four free parameters, $M_{200}$, $c$, $r_{\rm mis}$, and $f_{\rm mis}$, we calculate the Pearson correlation coefficient (PCC) for each subsample using Equation (14). The MCMC output of step 2, as described in Section 4.1, are used. As shown in Figure 5, the absolute PCC value is $<0.5$ for all subsamples, except the one between $r_{\rm mis}$ and $f_{\rm mis}$. The correlation between these two parameters is expected, as both

[14] http://www.shao.ac.cn/dhzhao/mandc.html

**Table 5**
Compilation of Previous Studies on the Measurement of the $c$–M Relation with Observation

| $z$ | $M_{\rm halo}(10^{14}\,M_\odot/h)$ | $N_{\rm halo}$ | $\sigma_M(10^{14}\,M_\odot/h)$ | $\sigma_c$ | References |
|---|---|---|---|---|---|
| 0.1–0.3 | $0.005–10^{b}$ | 222 699 | $\sim0.0867^{b}$ | $\sim2.997^{b}$ | Mandelbaum et al. (2008) |
| 0.1–0.6 | $0.48–3.21^{c}$ | 1 176 | $0.185^{c}$ | $5.4^{c}$ | Covone et al. (2014) |
| 0.19–0.69 | $6.9–37.1^{m}$ | 20 | $0.095^{c}$ | $0.335^{c}$ | Umetsu et al. (2014) |
| 0.19–0.89 | $0.53–1.56^{c}$ | 19 | $0.8^{c}$ | $1.0^{c}$ | Merten et al. (2015) |
| 0.2–0.4 | $0.05–2.00^{c}$ | 7 425 | $0.06^{c}$ | $0.91^{c}$ | low-$z$ in Shan et al. (2017) |
| 0.4–0.6 | $0.05–2.00^{c}$ | 27 358 | $0.05^{c}$ | $0.86^{c}$ | high-$z$ in Shan et al. (2017) |
| 0.08–0.35 | $0.05–5^{m}$ | 301 496 | $0.0308^{m}$ | $0.093^{m}$ | low-$z$ in this work |
| 0.35–0.65 | $0.05–5^{m}$ | 747 376 | $0.0394^{m}$ | $0.108^{m}$ | high-$z$ in this work |

**Note.** In the first three columns, the redshift range, the halo mass, and the halo number are shown in sequence. The uncertainties of the halo mass and the concentration are listed in the fourth and fifth columns. The last column shows the corresponding reference. The superscripts $c$, m, or b denote the total mass enclosed within a sphere of radius $r_{200c}$, $r_{200m}$, or $r_{200b}$, respectively, within which the mean density is 200 times of the critical, mean matter background, or mean baryon background density of the universe at the cluster redshift.

of them contribute to the miscentering effect.

$$\rho_{\rm X,Y} = \frac{\rm Cov(X,\,Y)}{\sigma_{\rm X}\sigma_{\rm Y}}. \tag{14}$$

## 6. Conclusion

With the DECaLS DR8 data, we extract and fit the stacked weak lensing signal of the halos in the redMaPPer, LOWZ, and CMASS catalogs. Using the model of the central halo, nearby halo, and miscentering effect, we model the weak lensing signal and get the value of halo mass and concentration for subsamples in multiple redshift and mass bins. We obtain the $c$–M relation for the halos with masses ranging from $10^{13}$ to $10^{15}\,M_\odot$ and redshifts ranging from $z=0.08$ to $z=0.65$. Compared with the power-law model, our fitting of the $c$–M relation prefers the K16 model (Klypin et al. 2016), which includes a trend of upturn after the pivot point of $\sim10^{14}\,M_\odot$. This is the first measurement of the $c$–M relation with DECaLS DR8 data. Our measurement shows the halo concentration with similar redshift decreases as the mass increases, except for the upturn at the massive end, which happens at lower masses for high-redshift halos. For halos with similar mass, the halo at large redshift has a larger concentration.

In this paper, we measure the $c$–M relation to detect the possible upturn at the high-mass end. There is still no consensus on the existence of or the reason for the upturn in the $c$–M relation. Some studies claim it comes from the unrelaxed dynamical state of the dark matter halo (Ludlow et al. 2012). Some others take the selection effect as the main contribution (Meneghetti & Rasia 2013). Some more studies explain the high concentration of massive clusters as a consequence of the alignment of the major axis of the ellipsoidal halo and the line of sight (e.g., Corless et al. 2009; Limousin et al. 2013; Sereno et al. 2013, 2018), assuming the shape of dark matter halo as triaxial instead of spherical.

In addition, there is a possible degeneracy between $f_{\rm mis}$ and $c$. An overestimated factor of miscentered halo is likely to overestimate the concentration. This would happen more frequently at high redshifts. Thus, to get more accurate constraints on the halo concentration, we need a better centering strategy, such as the massive galaxies near X-ray centroids (George et al. 2012). With the miscentering effect limited, the concentration and the $c$–M relation would be measured more accurately.

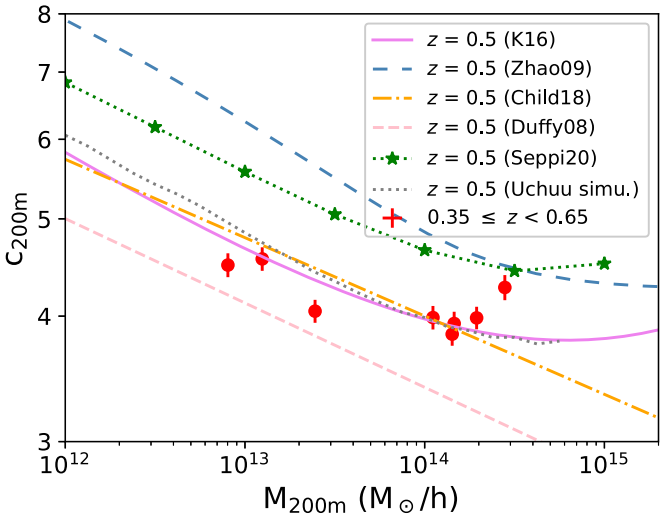


**Figure 4.** The comparison between our measurement for the high-redshift sample ($z2$ sample, $0.35 \leqslant z < 0.65$ and cosmological predictions for a halo at a redshift of 0.5. The red data points refer to our high-$z$ measurement, with lines for kinds of cosmological predictions of halos at a redshift of 0.5. For the abbreviation, *K16* refers to Klypin et al. (2016), *Child18* to Child et al. (2018), *Duffy08* to Duffy et al. (2008), *Seppi20* to Seppi et al. (2021), and *Uchuu simu.* to Ishiyama et al. (2021). The *Uchuu simu.* concentration used here is obtained with profile fitting.

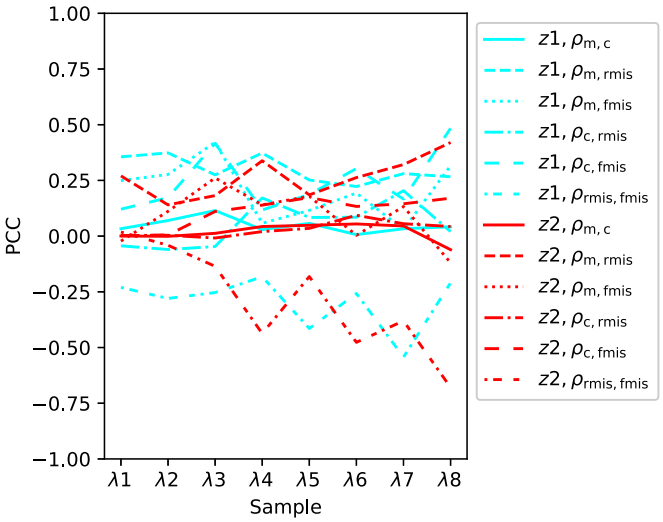


**Figure 5.** The PCC value for subsamples.

Furthermore, the upturn of the $c$–M relation can also be explained by the major mergers of massive clusters, when the subhalo moves to the central part radially and increases the concentration of the resulting halo (Klypin et al. 2011; Prada et al. 2012; Klypin et al. 2016). In our measurement, the K16 model (Klypin et al. 2016) with an upturn at the massive regime shows a comparatively good fitting, suggesting that a trend of upturn exists. This measurement is important for structure formation at the high-mass end. We expect that the next generation of weak lensing surveys, such as Euclid (Euclid Collaboration et al. 2019), LSST (LSST Science Collaboration et al. 2009), and CSST (Zhan 2011), will provide enough statistics to confirm and explain the existence of the upturn of the $c$–M relation at the high-mass end.

We acknowledge support from the National Key R&D Program of China (2016YFA0400703) and the National Science Foundation of China (11721303, 11890693). W.X. would like to thank Jin Wu, Siwei Zou, Junjie Jin, Yu Qiu, Shu Wang, and Zhiwei Pan for useful help and discussions during the development of this paper. H.Y.S. acknowledges the support from NSFC of China under grant 11973070, the Shanghai Committee of Science and Technology grant No. 19ZR1466600, and Key Research Program of Frontier Sciences, CAS, grant No. ZDBS-LY-7013. RL acknowledge the support of National Nature Science Foundation of China (Nos 11988101, 11773032, 12022306), the science research grants from the China Manned Space Project (Nos CMS-CSST-2021-B01, CMS-CSST-2021-A01) and the support from K.C. Wong Education Foundation.

*Software: Cluster toolkit* (Smith et al. 2003; Eisenstein & Hu 1998; Takahashi et al. 2012), *CAMB* (Challinor & Lewis 2011; Lewis et al. 2000), *SWOT* (Coupon et al. 2012), *EMCEE* (Foreman-Mackey et al. 2013), *WebPlotDigitizer* (Rohatgi 2020).

## ORCID iDs

Weiwei Xu https://orcid.org/0000-0002-9587-6683
Huanyuan Shan https://orcid.org/0000-0001-8534-837X

## References

Abbott, T. M. C., Abdalla, F. B., Alarcon, A., et al. 2018, PhRvD, 98, 043526
Abbott, T. M. C., Aguena, M., Alarcon, A., et al. 2020, PhRvD, 102, 023509
Ahn, C. P., Alexandroff, R., Allende Prieto, C., et al. 2014, ApJS, 211, 17
Bardeen, J. M., Bond, J. R., Kaiser, N., & Szalay, A. S. 1986, ApJ, 304, 15
Bhattacharya, S., Habib, S., Heitmann, K., & Vikhlinin, A. 2013, ApJ, 766, 32
Bielby, R. M., Finoguenov, A., Tanaka, M., et al. 2010, A&A, 523, A66
Blum, R. D., Burleigh, K., Dey, A., et al. 2016, AAS Meeting Abstracts, 228, 317.01
Bullock, J. S., Kolatt, T. S., Sigad, Y., et al. 2001, MNRAS, 321, 559
Buote, D. A., Gastaldello, F., Humphrey, P. J., et al. 2007, ApJ, 664, 123
Cardamone, C. N., van Dokkum, P. G., Urry, C. M., et al. 2010, ApJS, 189, 270
Challinor, A., & Lewis, A. 2011, PhRvD, 84, 043516
Child, H. L., Habib, S., Heitmann, K., et al. 2018, ApJ, 859, 55
Comerford, J. M., & Natarajan, P. 2007, MNRAS, 379, 190
Corless, V. L., King, L. J., & Clowe, D. 2009, MNRAS, 393, 1235
Coupon, J., Kilalinger, M., McCracken, H. J., et al. 2012, A&A, 542, A5
Covone, G., Sereno, M., Kilbinger, M., & Cardone, V. F. 2014, ApJL, 784, L25
Cui, W., Knebe, A., Yepes, G., et al. 2018, MNRAS, 480, 2898
Dark Energy Survey Collaboration, Abbott, T., Abdalla, F. B., et al. 2016, MNRAS, 460, 1270
Dey, A., Schlegel, D. J., Lang, D., et al. 2019, AJ, 157, 168
Duffy, A. R., Schaye, J., Kay, S. T., & Dalla Vecchia, C. 2008, MNRAS, 390, L64
Eisenstein, D. J., & Hu, W. 1998, ApJ, 496, 605
Eke, V. R., Navarro, J. F., & Steinmetz, M. 2001, ApJ, 554, 114
Euclid Collaboration, Martinet, N., Schrabback, T., et al. 2019, A&A, 627, A59
Foreman-Mackey, D., Hogg, D. W., Lang, D., & Goodman, J. 2013, PASP, 125, 306
Gastaldello, F., Buote, D. A., Humphrey, P. J., et al. 2007, ApJ, 669, 158
George, M. R., Leauthaud, A., Bundy, K., et al. 2012, ApJ, 757, 2
Giblin, B., Heymans, C., Asgari, M., et al. 2021, A&A, 645, A105
Hildebrandt, H., Viola, M., Heymans, C., et al. 2017, MNRAS, 465, 1454
Hoekstra, H., Franx, M., Kuijken, K., & van Dokkum, P. G. 2002, MNRAS, 333, 911
Ishiyama, T., Prada, F., Klypin, A. A., et al. 2021, MNRAS, 506, 4210
Johnston, D. E., Sheldon, E. S., Wechsler, R. H., et al. 2007, arXiv:0709.1159
Klypin, A., Yepes, G., Gottlöber, S., Prada, F., & Heß, S. 2016, MNRAS, 457, 4340
Klypin, A. A., Trujillo-Gomez, S., & Primack, J. 2011, ApJ, 740, 102
Kwan, J., Sánchez, C., Clampitt, J., et al. 2017, MNRAS, 464, 4045
Laigle, C., McCracken, H. J., Ilbert, O., et al. 2016, ApJS, 224, 24
Lang, D., Hogg, D. W., & Schlegel, D. J. 2016, AJ, 151, 36
Lewis, A., Challinor, A., & Lasenby, A. 2000, ApJ, 538, 473
Limousin, M., Morandi, A., Sereno, M., et al. 2013, SSRv, 177, 155
LSST Science Collaboration, Abell, P. A., Allison, J., et al. 2009, arXiv:0912.0201
Ludlow, A. D., Navarro, J. F., Li, M., et al. 2012, MNRAS, 427, 1322
Mandelbaum, R., Seljak, U., Cool, R. J., et al. 2006, MNRAS, 372, 758
Mandelbaum, R., Seljak, U., & Hirata, C. M. 2008, JCAP, 2008, 006
McClintock, T., Varga, T. N., Gruen, D., et al. 2019, MNRAS, 482, 1352
Mehta, V., Scarlata, C., Capak, P., et al. 2018, ApJS, 235, 36
Melchior, P., Gruen, D., McClintock, T., et al. 2017, MNRAS, 469, 4899
Meneghetti, M., & Rasia, E. 2013, arXiv:1303.6158
Merten, J., Meneghetti, M., Postman, M., et al. 2015, ApJ, 806, 4
Miller, L., Kitching, T. D., Heymans, C., Heavens, A. F., & van Waerbeke, L. 2007, MNRAS, 382, 315
Miller, L., Heymans, C., Kitching, T. D., et al. 2013, MNRAS, 429, 2858
Moraes, B., Kneib, J. P., Leauthaud, A., et al. 2014, RMxAA, 27, 202
Navarro, J. F., Frenk, C. S., & White, S. D. M. 1995, MNRAS, 275, 56
Navarro, J. F., Frenk, C. S., & White, S. D. M. 1996, ApJ, 462, 563
Navarro, J. F., Frenk, C. S., & White, S. D. M. 1997, ApJ, 490, 493
Neto, A. F., Gao, L., Bett, P., et al. 2007, MNRAS, 381, 1450
Phriksee, A., Jullo, E., Limousin, M., et al. 2020, MNRAS, 491, 1643
Planck Collaboration, Aghanim, N., Akrami, Y., et al. 2020, A&A, 641, A6
Pointecouteau, E., Arnaud, M., & Pratt, G. W. 2005, AdSpR, 36, 659
Prada, F., Klypin, A. A., Cuesta, A. J., Betancort-Rijo, J. E., & Primack, J. 2012, MNRAS, 423, 3018
Rohatgi, A. 2020, Webplotdigitizer: Version 4.4, https://automeris.io/WebPlotDigitizer
Rykoff, E. S., Rozo, E., Busha, M. T., et al. 2014, ApJ, 785, 104
Sato, S., Akimoto, F., Furuzawa, A., et al. 2000, ApJL, 537, L73
Seppi, R., Comparat, J., Nandra, K., et al. 2021, A&A, 652, A155
Sereno, M., Ettori, S., Umetsu, K., & Baldi, A. 2013, MNRAS, 428, 2241
Sereno, M., Giocoli, C., Ettori, S., & Moscardini, L. 2015, MNRAS, 449, 2024
Sereno, M., Umetsu, K., Ettori, S., et al. 2018, ApJL, 860, L4
Shan, H., Kneib, J.-P., Li, R., et al. 2017, ApJ, 840, 104
Shan, H., Kneib, J.-P., Tao, C., et al. 2012, ApJ, 748, 56
Sheldon, E. S., Johnston, D. E., Frieman, J. A., et al. 2004, AJ, 127, 2544
Smith, R. E., Peacock, J. A., Jenkins, A., et al. 2003, MNRAS, 341, 1311
Takahashi, R., Sato, M., Nishimichi, T., Taruya, A., & Oguri, M. 2012, ApJ, 761, 152
Umetsu, K., Medezinski, E., Nonino, M., et al. 2014, ApJ, 795, 163
Varga, T. N., Gruen, D., Seitz, S., et al. 2021, MNRAS, stab3269
Vikhlinin, A., Kravtsov, A., Forman, W., et al. 2006, ApJ, 640, 691
Yang, F., Chary, R.-R., & Liu, J.-F. 2020, arXiv:2012.08744
Yao, J., Shan, H., Zhang, P., Kneib, J.-P., & Jullo, E. 2020, ApJ, 904, 135
Zhan, H. 2011, SSPMA, 41, 1441
Zhao, D. H., Jing, Y. P., Mo, H. J., & Börner, G. 2003a, ApJL, 597, L9
Zhao, D. H., Jing, Y. P., Mo, H. J., & Börner, G. 2009, ApJ, 707, 354
Zhao, D. H., Mo, H. J., Jing, Y. P., & Börner, G. 2003b, MNRAS, 339, 12
Zou, H., Gao, J., Zhou, X., & Kong, X. 2019, ApJS, 242, 8
Zu, Y., Shan, H., Zhang, J., et al. 2021, MNRAS, 505, 5117